Supporting Information

Table of Contents:

S1. Structure Characterization.

S1.1. Single crystal X-Ray diffraction analysis of compound [Cu(NH$_2$-MeIN)I]$_n$ (2m)

The crystal structure of compound [Cu(NH$_2$-MeIN)I]$_n$ (**2m**) is formed by a very simple asymmetric unit (**Figure S1**). When it is expanded, a polymeric *stair-case* motif of copper-iodine is generated parallel to the *a*–axis (**Figure S2**).

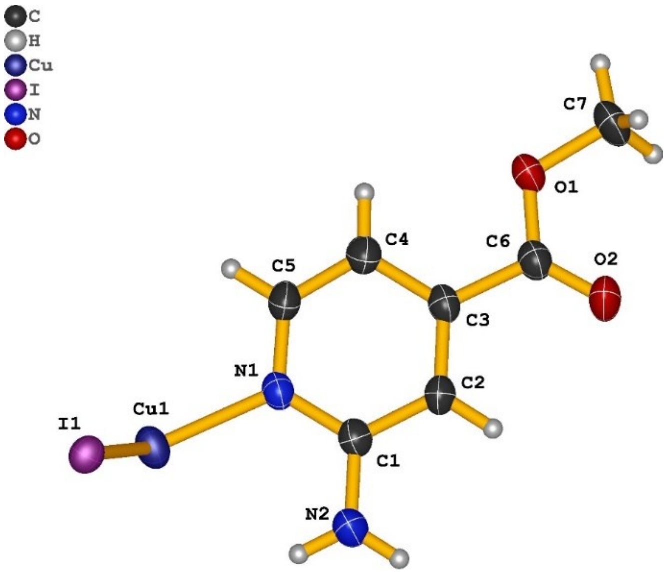

Figure S1. Thermal ellipsoid plot (50%) and labelling scheme for compound [Cu(NH$_2$-MeIN)I]$_n$ (**2m**) at room conditions.

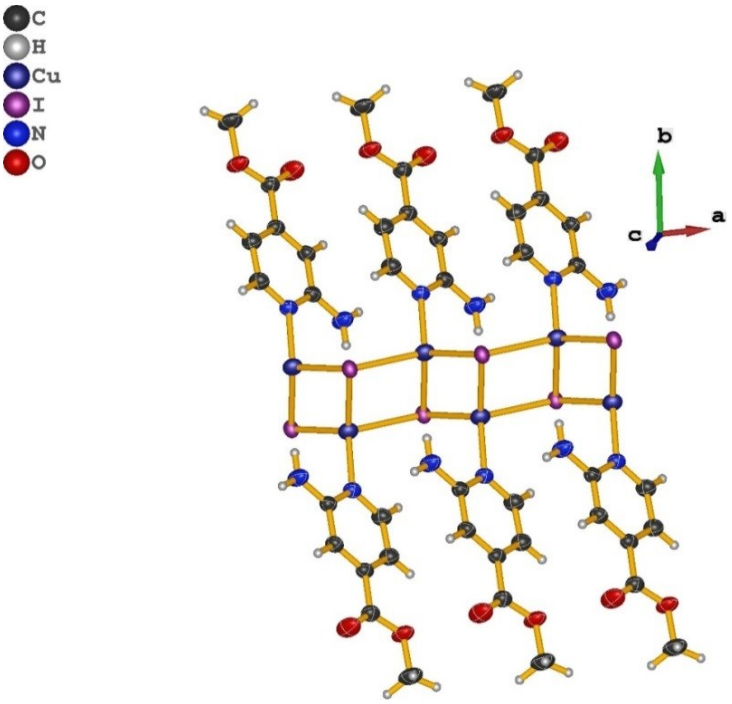

Figure S2. View of compound [Cu(NH$_2$-MeIN)I]$_n$ (**2m**) forming a 1D polymer stair-case parallel to the *a*-axis.

$[Cu(NH_2\text{-MeIN})I]_n$ (**2m**) presents each copper(I) atom four-coordinated, to three iodine atoms and the nitrogen of the organic ligand. The shape of this coordination environment can be described by a single geometric index[S1] called τ_4 that takes a value of 1.0 for perfect tetrahedral configuration while it will be 0.0 in the case of perfect square configuration. In the case of intermediate configurations such as trigonal pyramidal the τ_4 parameter will have a value between 0.0 and 1.0. In the compound under study the τ_4 is 0.86 indicating a distorted trigonal pyramidal configuration. The iodine atom is three-coordinated and the organic ligands preserve their planarity.

Geometric parameters for this compound at ambient conditions are similar to the values measured in similar stair-cases in copper iodine structures with organic ligands contained in the CSD Database (version 5.36)[S2]. We found 2.643(2)Å for Cu-I and 2.037(2)Å for Cu-N distances, respectively, in good agreement with the values 2.66(5)Å and 2.04(1)Å reported in CSD. For angles, the value for I-Cu-N in our polymer is 111.09(7)º while the average value obtained from CSD was 110(5)º. In the case of I-Cu-I angles, this parameter is characterized by a range from 93.02º to 119.37º. In the present compound these values are 99.05(7)º and 119.51(8)º. The shorter Cu···Cu distance is 2.682(4)Å and distances for the organic ring is 4.2503(17)Å (centroid – centroid).

S1.2. Single crystal X-Ray diffraction analysis of [Cu(MeIN)I]$_n$ **(1m)**[6] and [Cu(NH$_2$-MeIN)I]$_n$ **(2m) at different temperatures**.

Table S1. Lattice parameters of compound [Cu(NH$_2$-MeIN)I]$_n$ (**2m**) at 296 K (**2**^{RT}) and at 110 K (**2**^{LT}).

Compound	**2m^{RT}**	**2m^{LT}**
Empirical formula	$C_7H_8CuIN_2O_2$	$C_7H_8CuIN_2O_2$
Formula weight	342.59	342.59
T (K)	296	110
λ (Å)	0.71073	0.71073
Crystal system	Triclinic	Triclinic
Space group	*P*-1	*P*-1
a (Å)	4.2503(2)	4.2103(3)
b (Å)	10.1169(4)	9.9279(6)
c (Å)	11.3784(5)	11.2864(7)
α (°)	81.030(3)	82.189(3)
β (°)	88.843(3)	89.223(3)
γ (°)	82.580(4)	83.312(3)
V (Å^3)	479.24(4)	464.21(5)
Z	2	2
ρ_{calc} (g·cm^{-3})	2.374	2.451
μ (mm^{-1})	5.467	5.644
Reflections collected	2481	1691
Unique data/parameters	2481/127	1691/119
Goodness of fit (*S*)	1.036	1.319
*R*1/*wR*2 [*I*>2σ(*I*)]	0.0247/0.0477	0.0189/0.0548
*R*1/*wR*2 [all data]	0.0292/0.0493	0.0235/0.0740

Table S2. Bond distances (Å) and angles (°) of compound [Cu(NH_2-MeIN)I]$_n$ (**2m**) at 296 K (**2m**^{RT}) and at 110 K (**2m**^{LT}).

Compound	**2m**^{RT}	**2m**^{LT}
T (K)	296	110
Cu-I1$_{rail}$	2.643(2)	2.6257(6)
Cu-I1$^{i}_{rail}$	2.733(2)	2.7181(6)
Δ[Cu-I1$_{rail}$]	0.090	0.0924
Cu-I1$_{rung}$	2.680(2)	2.6682(6)
Cu-N1	2.04(1)	2.028(4)
Cu-Cu^{ii}	2.682(4)	2.627(1)
Cu-Cu^{iii}	3.514	3.523
Δ[Cu-Cu]	0.832	0.896
I1-Cu1-I1^{i}	104.33(8)	103.96(2)
I1-Cu1-I1^{ii}	99.05(7)	98.31(2)
I1^{i}-Cu1-I1^{i}	119.51(8)	120.50(2)
Cu1-I1-Cu1^{ii}	80.95(7)	81.69(2)
Cu1-I1-Cu1^{iii}	104.34(8)	103.96(2)
Cu1^{ii}-I1-Cu1^{ii}	60.49(8)	59.50(2)
Dihedral angle	112.22	111.65
Tilt angle	87.47	88.19
Twist angle	53.52	52.87

Symmetry codes: i) x-1, y, z; ii) -x, -y, -z+1; iii) -x+1, -y, -z+1

S1.3. High pressure single crystal X-Ray diffraction analysis of compound [Cu(NH$_2$-MeIN)I]$_n$ (2m).

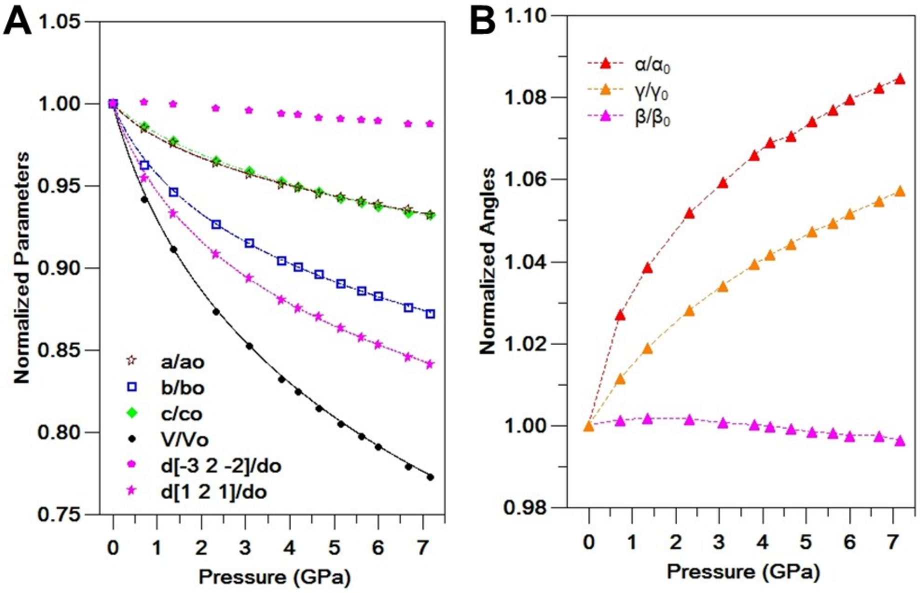

Figure S3. Variation of the cell distances and volume (a) and angles (b) of [Cu(NH$_2$-MeIN)I]$_n$ (**2m**) with pressure. Error bars are smaller than their respective size symbols. Curve lines in (a) correspond to the respective EoS model fit.

Evolution of all unit cell parameters is smooth up to the maximum pressure achieved. The *b*-axis is substantially softer than *a* and *c*-axes while the *α* angle is the most variable angle and *β* angle remains almost unchanged but with a maximum around 1.5 GPa. The softest direction found for this compound is [1 2 1] as is showed on Figure S3a.

For EoS calculations we have selected the 3rd-order Birch-Murnaghan (BM) according to the information obtained from the plots of the axes and *V* unit-cell parameters as normalized pressure (*F*) pressure against finite strain (*f*) (i.e. *f-F* plots, Figure S4). The *f-F* plots for unit-cell parameters exhibit a curvature at low pressures indicating that values at zero pressure are not strictly consistent with the higher-pressure data. However, comparison of data collected from crystals within the DAC but without pressure fluid and data from crystals in air, shows that the formal uncertainties obtained for the unit-cell parameters are underestimated, and this accounts for the observed curvature in the *f-F* plots.

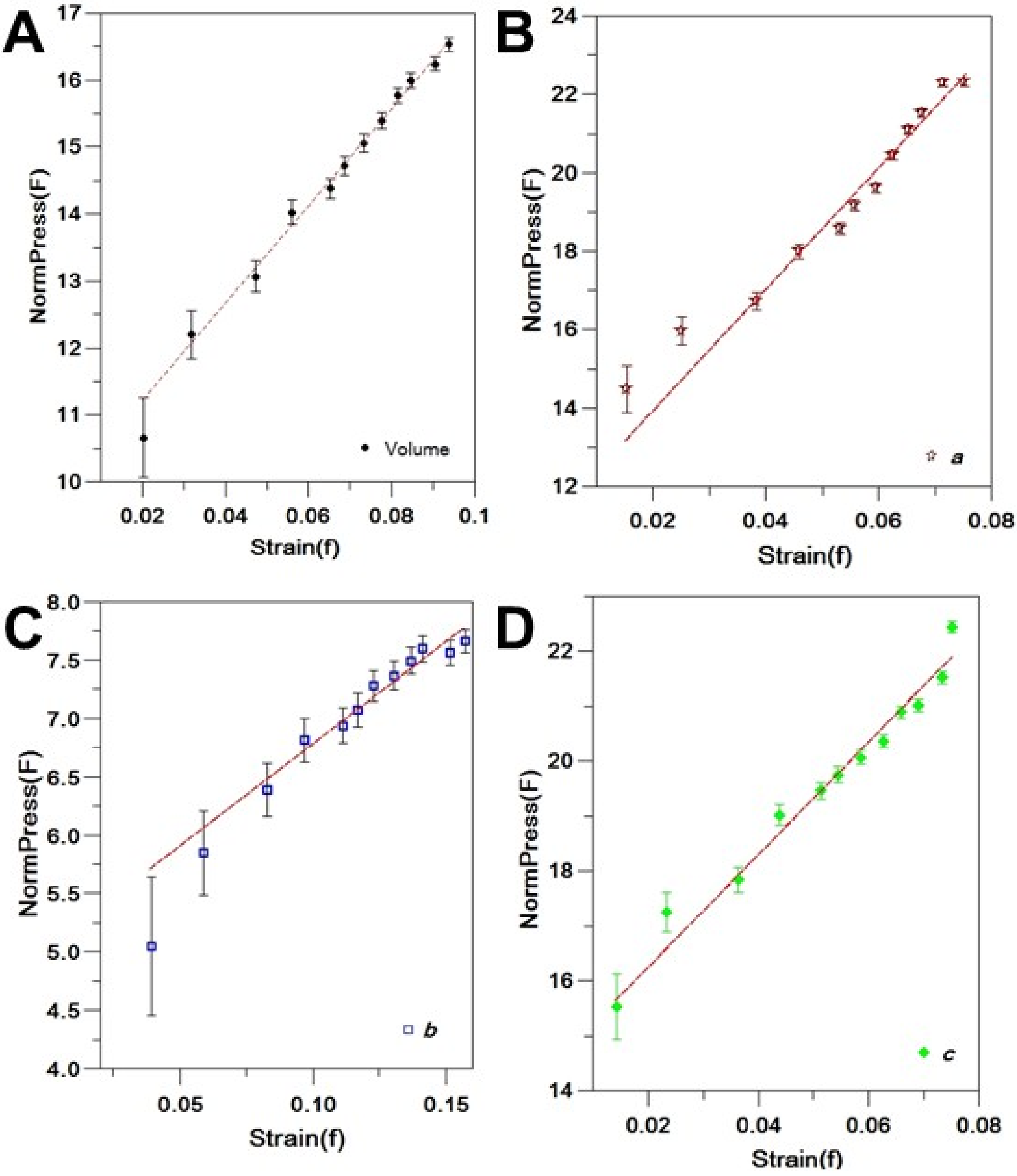

Figure S4. *f-F* plots for Volume (a) and cell parameters (b-d) for $[Cu(NH_2\text{-}MeIN)I]_n$ (**2m**).

The volume (*V*) and cell parameters (*a*, *b* and *c*) at equilibrium are displayed as V_0 and L_0, in Table S3, linear and bulk moduli M_0 and K_0, both in GPa, and their first derivative M'_0 and K'_0 for each axis and the bulk respectively. The fitting procedure was done with the ***EosFit7-GUI*** programme[S3] using the BM EoS, with the linear modification of Angel *et al.* used to fit individual cell parameters and directions. The refinements of EoS all yield $w\chi^2 < 1$ because of the over-estimation of the $\sigma(P)$, but none of the fits show any systematic variation of P_{obs}-P_{Calc} with pressure, indicating that the reported parameters represent the data well. Lines on Figure S3a show the fitted EoS models.

Table S3. EoS parameters for $[Cu(NH_2\text{-}MeIN)I]_n$ (**2m**).

	EoS Model	L_0	M_0	M'_0
A	*BM3*	4.25029(3)	32(2)	40(3)
b	*BM3*	10.1169(6)	15.1(6)	19.0 (8)
c	*BM3*	11.3784(8)	42 (2)	26(2)
[1 2 1]	*BM3*	25.5519 (8)	12.4(3)	13.8(3)
		V_0	K_0	K'_0
V	*BM3*	479.24(4)	9.7 (2)	9.0 (3)

These fits (Table S3) confirm that the hydrostatic compression of this material is very anisotropic, with the *b-axis* being much softer than the other two unit-cell axes. However, this material is triclinic and therefore the compression of the unit-cell axes alone does not necessarily represent the true compressibility tensor. The true pattern of compressibility is represented by the strain ellipsoid due to compression; two of the principal axes of this ellipsoid represent the directions of minimum and maximum compression, which can rotate with respect to the unit-cell axes during compression. The principal strains from the measured unit-cell parameters at each pressure and the room-pressure unit-cell were calculated with the Win_Strain programme[S4] We used the Eulerian finite strain definition because this is the same as used for BM EoS calculations; the orientation of the strain ellipsoid is not sensitive to the choice of strain definition. The softest direction was determined as [1 2 1] direction and not so far with values obtained for the *b*-axis.

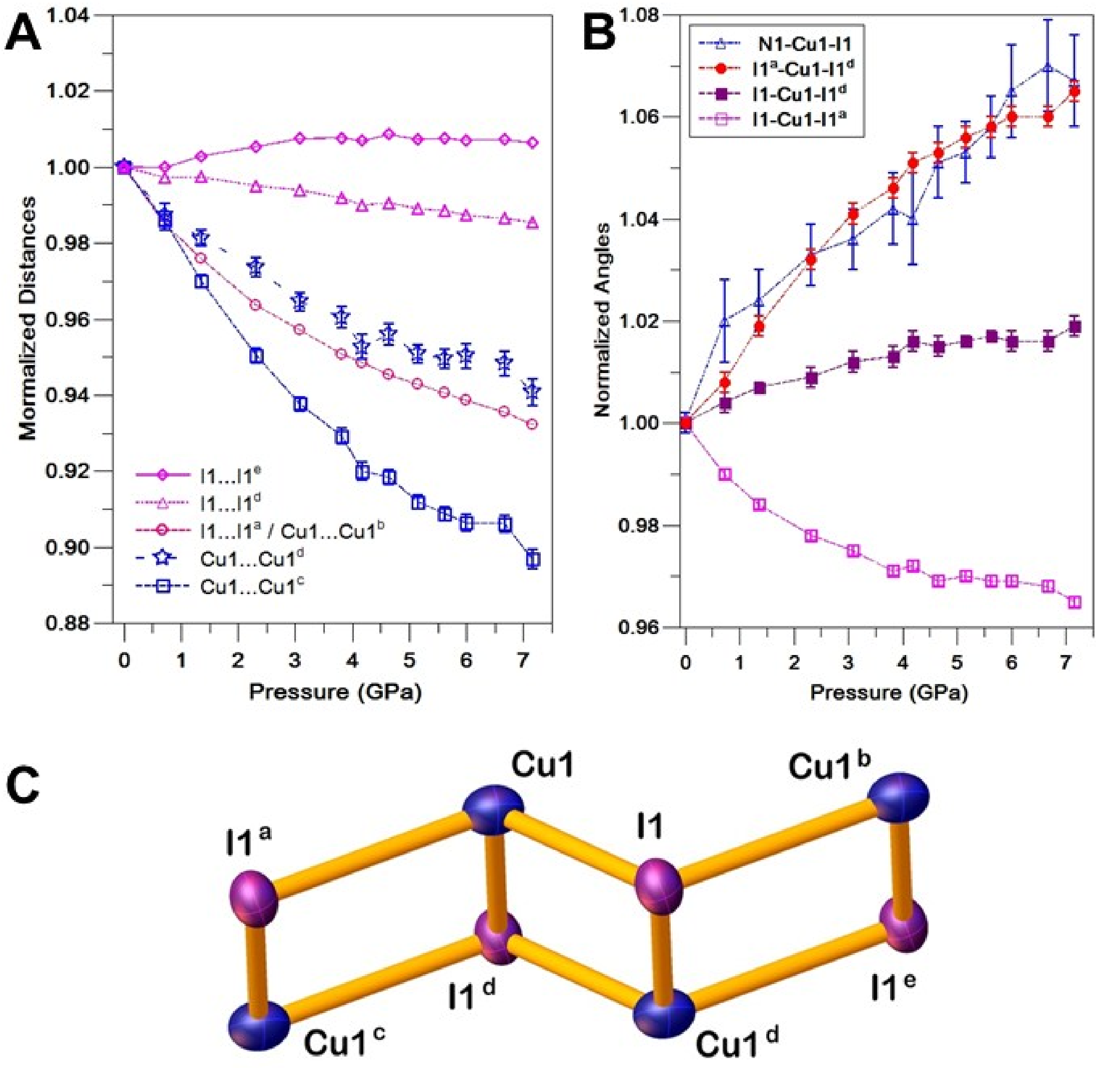

Figure S5. Variation of the Cu···Cu and I···I distances (a) and angles (b) of **2m** with pressure. Error bars represent the standard for each value. Symmetry codes: ***a***: -1+*x*, *y*, *z*; ***b***: 1+*x, y*, *z*; ***c***: 1-*x*,-*y*,1-*z*; ***d***: 2-*x*,-*y*,1-*z*; ***e***: 3-*x*,-*y*,1-*z.* c) Schematic representation of the Cu_2-I_2 chain in **2m**.

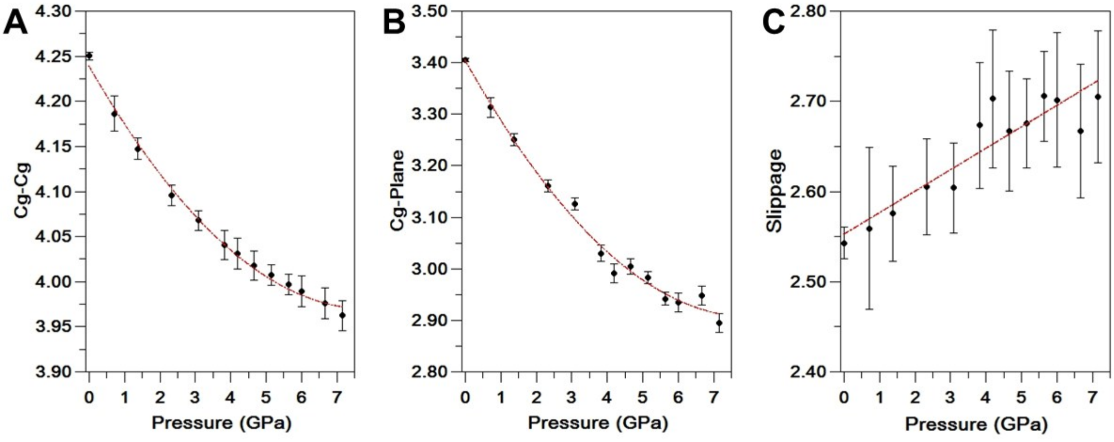

Figure S6. Perpendicular distances between layers (a, b) and their respective mutual slippage (in-plane component of relative displacement) (c) with pressure.

S1.3. X-ray powder diffraction analysis of [Cu(MeIN)I]$_n$ (1m and 1n) and [Cu(NH$_2$-MeIN)I]$_n$ (2m and 2n).

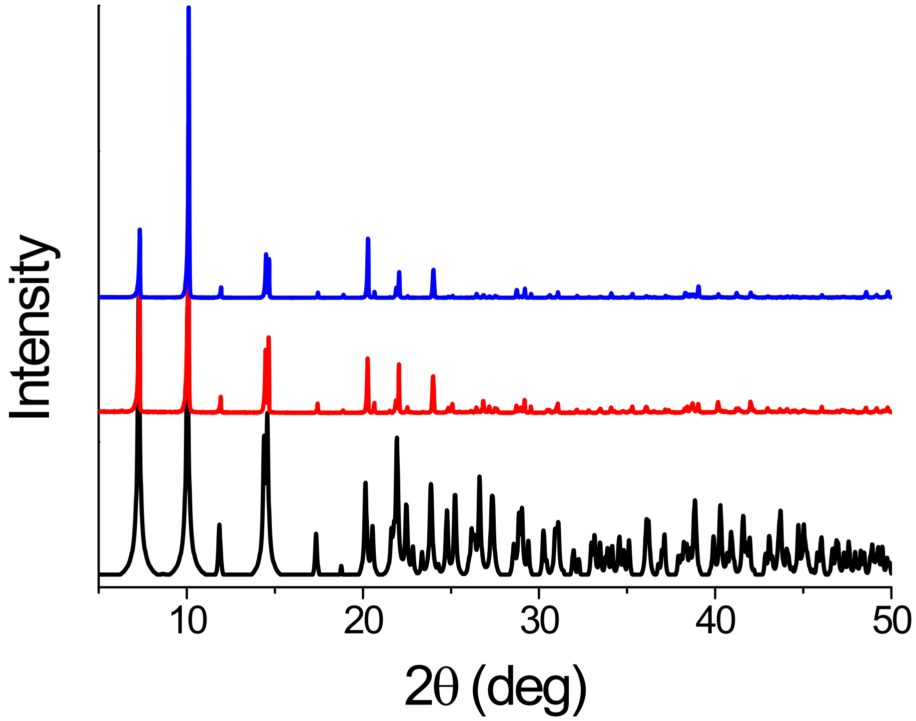

Figure S7. X-ray powder diffractograms of compound [Cu(MeIN)I]$_n$: theoretical (black), **1m** microcrystals (red),[6] **1n** nanofibers (blue).

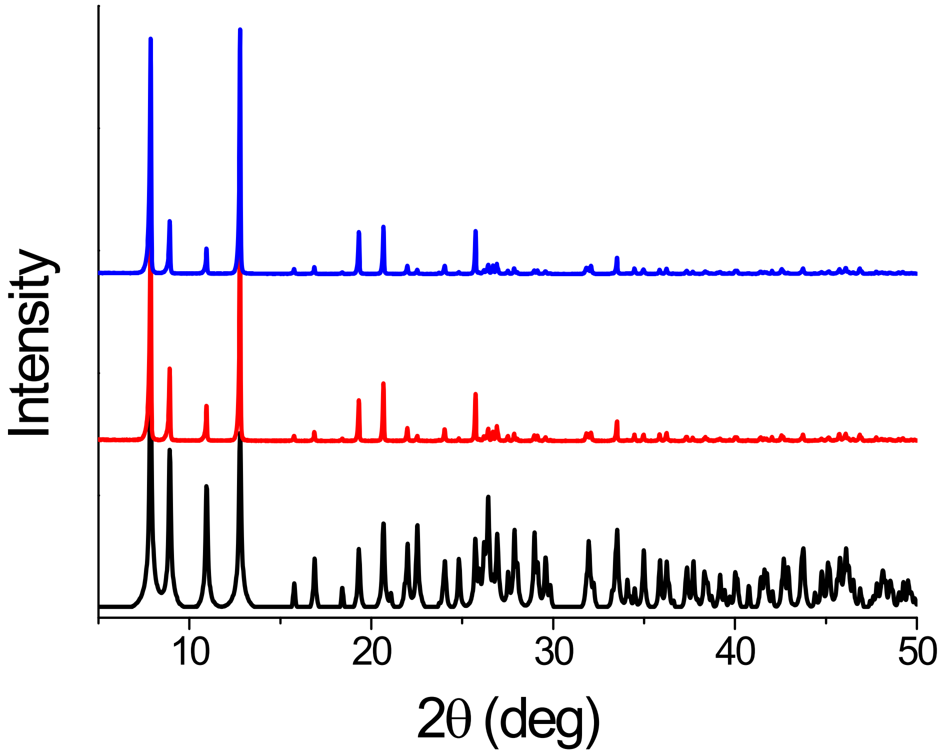

Figure S8. X-ray powder diffractograms of compound [Cu(NH$_2$-MeIN)I]$_n$: theoretical (black), **2m** crystals (red), **2n** nanofibers (blue).

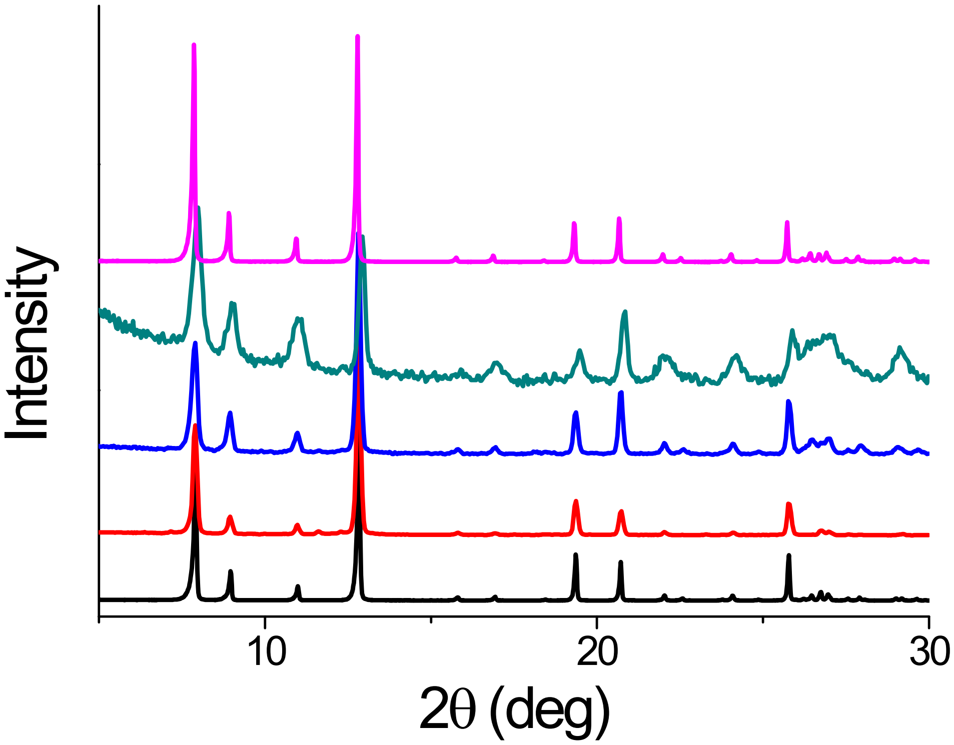

Figure S9. X-ray powder diffractograms of compound [Cu(NH$_2$-MeIN)I]$_n$: **2n** nanofibers (black), pellets prepared at pressures of 1 GPa (red), 3 GPa (blue) and 5 GPa (green), and a ground pellet (pink).

S2. Morphological Characterization

S2.1. AFM of $[Cu(NH_2\text{-MeIN})I]_n$ (2n).

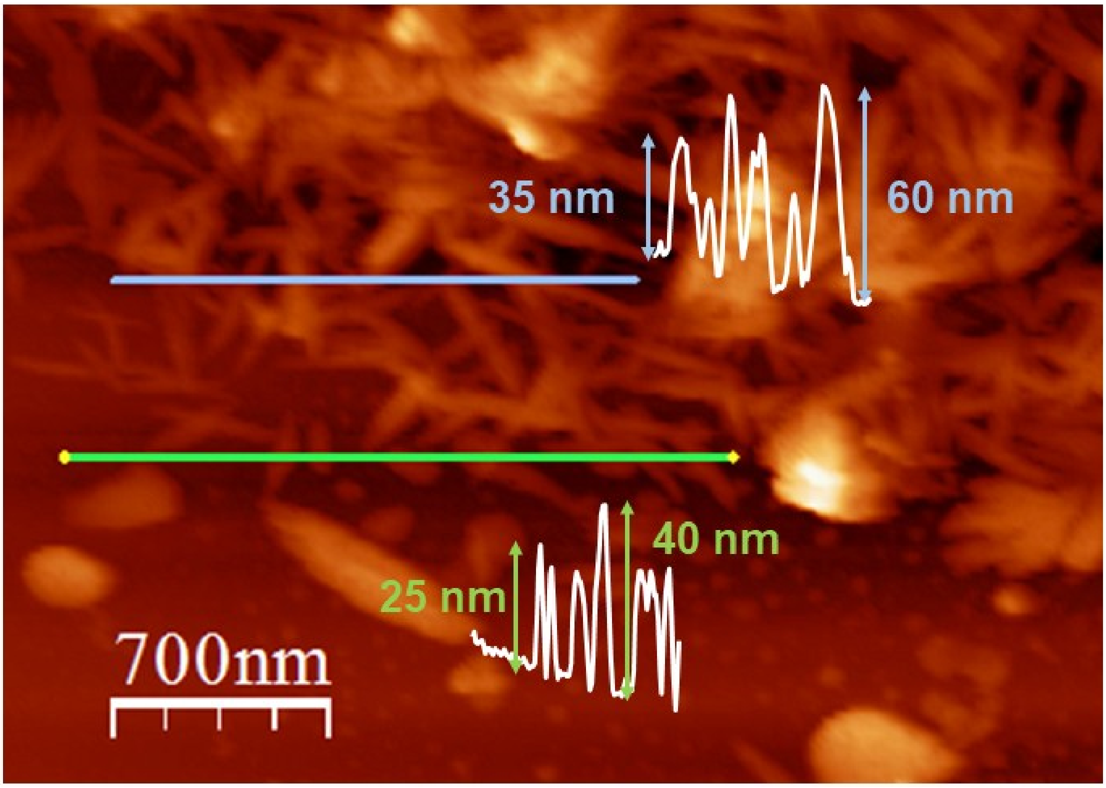

Figure S10. AFM image of isolated **2n** nanofibers on SiO_2 prepared by drop casting, with their height profiles along the blue and green lines.

S3. Thermogravimetric analysis of [Cu(MeIN)I]$_n$ (1m) and [Cu(NH$_2$-MeIN)I]$_n$ (2m).

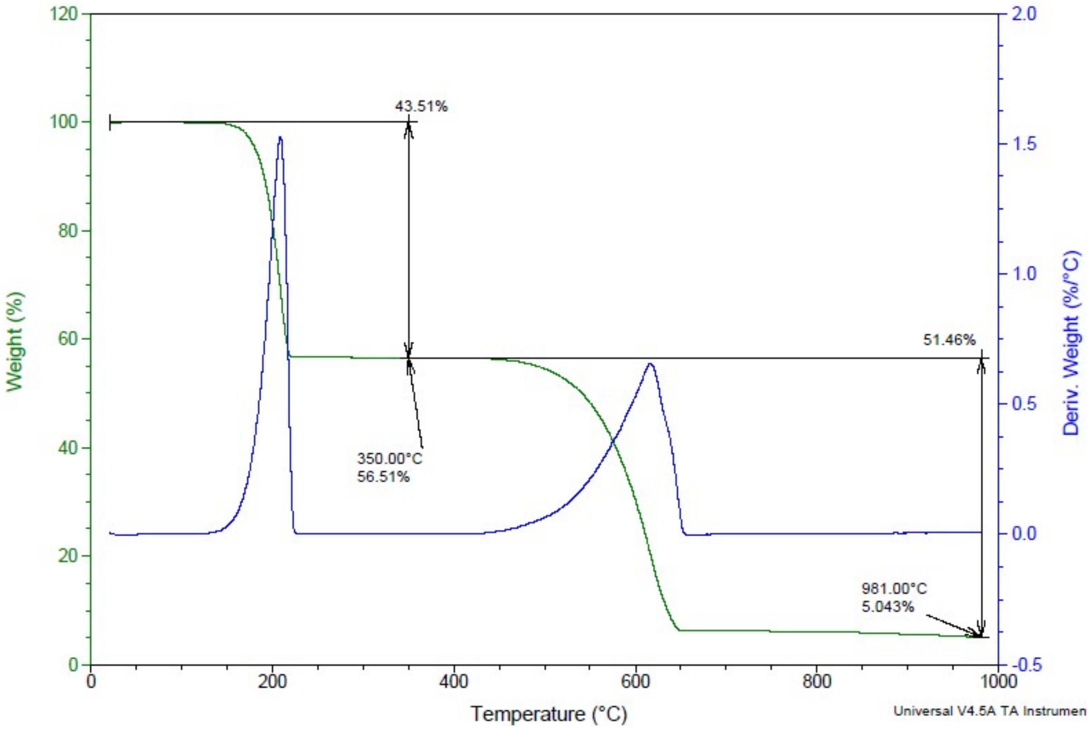

Figure S11. Thermogravimetric analysis of compound **2** under nitrogen gas with flow rate 90 mL/min and heating rate 10 ºC/min.

Both compounds decompose following the same mechanism: from 100 to 300 ºC, we see a first weight loss which corresponds to the ligand (methyl isonicotinate for compound **1m**[6] and methyl 2-aminoisonicotinate for compound **2m**). The second loss, which occurs from 400 to 700 ºC, corresponds to iodine and some volatile copper-iodine compounds.

This behaviour is observed for both micrometric crystals and nanometric fibres of these compounds.

S4. Emission studies of [Cu(MeIN)I]$_n$ (1m) and [Cu(NH$_2$-MeIN)I]$_n$ (2m).

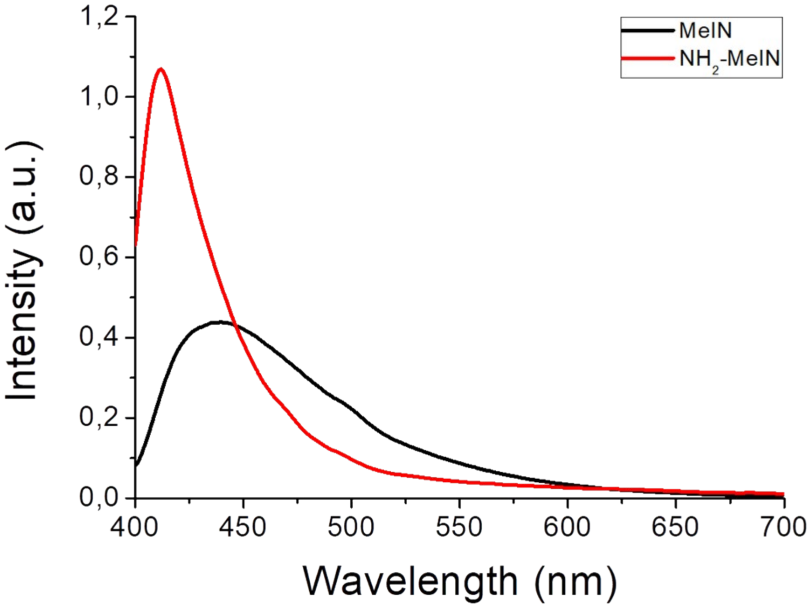

Figure S12. Luminescence spectra of MeIN (black) and NH$_2$-MeIN (red) at 300 K.

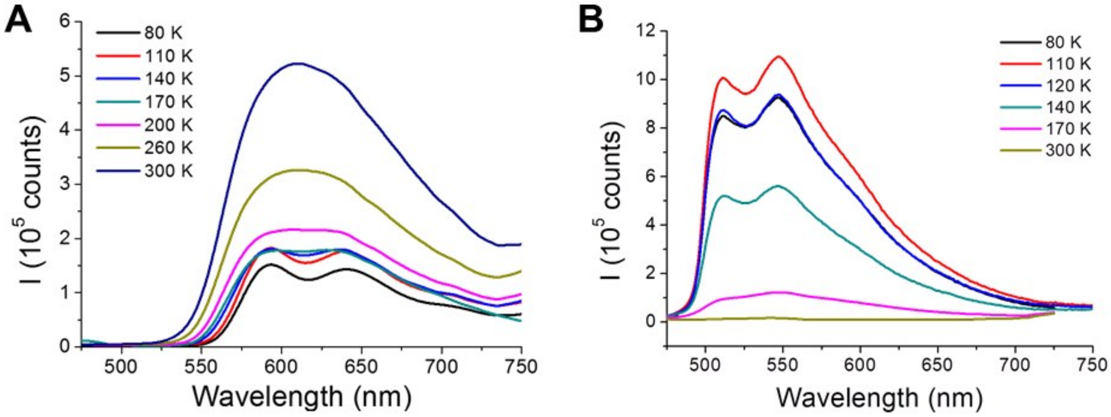

Figure S13. a) Emissive behavior at variable temperature of microcrystals of [Cu(MeIN)I]$_n$ (**1m**) and [Cu(NH$_2$-MeIN)I]$_n$ (**2m**), respectively.

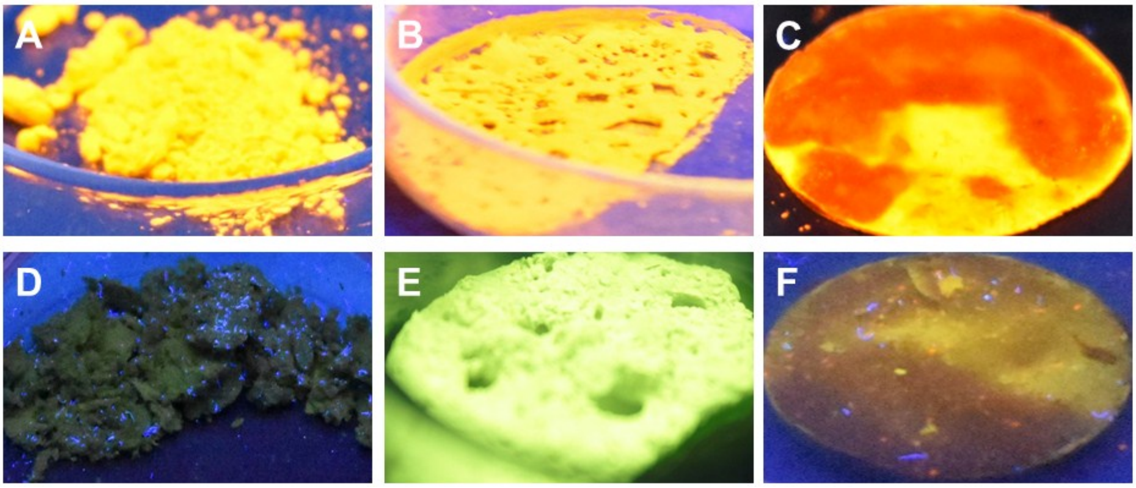

Figure S14. (a, b, c) Luminescence of **1n** at 298 K (a), at 80 K (b) and at 80 K and 2 GPa (c). (d, e, f) Luminescence of **2n** at 298 K (d), at 80 K (e) and at 80 K and 2 GPa (f). λ_{exc} = 312 nm.

Table S4. Most representative variation in the Cu-Cu distances and I-Cu-I and Cu-I-Cu angles for compound **2m**, from 0 to 7.16 GPa.

Bonds (Å) and Angles (°)	298 K, 0 GPa	298 K, 7.16 GPa	Δ
Cu-Cu^{ii}	2.682(4)	2.53(1)	-0.15 (5.60 %)
Cu-Cu^{iii}	3.514	3.151	-0.363 (10.33 %)
I1-Cu1-I1^{i}	104.33(8)	100.7(1)	-3.6 (3.45 %)
I1-Cu1-I1^{ii}	99.05(7)	105.5(2)	+6.5 (6.56 %)
I1^{i}-Cu1-I1^{i}	119.51(8)	121.7(3)	+2.2 (1.84 %)
Cu1-I1-Cu1^{ii}	80.95(7)	74.5(2)	-6.5 (8.03 %)
Cu1^{ii}-I1-Cu1^{ii}	60.49(8)	58.3(3)	-2.2 (3.64 %)

Symmetry codes: i) x-1, y, z; ii) -x, -y, -z+1; iii) -x+1, -y, -z+1

Table S5. Most representative distances (Å) and angles (°) of the ligand residues for compound **2m** at different temperatures.

Compound	**2m^{RT}**	**2m^{LT}**
T (K)	296	110
C1-N2	1.355(4)	1.368(5)
C6-O2	1.200(3)	1.212(5)
C6-O1	1.326(4)	1.324(5)
H-bond distance (N-H···O)	2.306	2.239
H-bond angle (N-H···O)	153.48	156.25

When lowering the temperature from 296 to 110 K, apart from the Cu_2I_2 double chains, the ligand residues of compound **2m** are also affected. The C-N distances between the amino groups and the pyridinic rings increase, and so do the C=O distances of the carboxylate groups. Thus, the hydrogen bond distances decrease and their angles slightly increase. Still, this variation is not so important as to outstand the effect of the reduction of Cu···Cu distances in the thermochromic behaviour of the CP.

S5. Electrical behaviour study of $[Cu(NH_2\text{-}MeIN)I]_n$ (2m).

The thermal dependence of the electrical resistivity of a single crystal of compound **2** shows that, initially, this compound is almost an insulator at room temperature, with an extrapolated conductivity value of *ca*. 10^{-15} S/cm. When the sample is heated from room temperature to 400 K, the resistance remains above the detection limit of our equipment (5×10^{11} Ω) up to *ca*. 360 K and, accordingly, the resistivity (ρ) shows a constant value below this temperature. Above *ca*. 360 K the resistivity decreases and reaches a value of *ca*. 3.2×10^{6} Ω cm at 400 K (i.e., $\sigma = 1/\rho = 3.1\times10^{-7}$ S cm^{-1}). Interestingly, at 400 K the resistivity decreases with time and after *ca*. 10 min at 400 K the resistivity reaches a constant value of *ca*. 3×10^{3} Ω cm ($\sigma = 3.3\times10^{-4}$ S cm^{-1}). Once the resistivity value is stabilized, the temperature was decreased to 2 K. In this cooling scan the resistivity shows a quasi-metallic behaviour and initially decreases to reach a broad minimum at *ca*. 225 K with a value of *ca*. 8×10^{2} Ω cm (Figure S15a). Below this temperature the resistivity increases to reach a value of *ca*. 3×10^{8} Ω cm at 2 K. If the crystal is heated from 2 to 400 K the resistivity shows the same values observed in the cooling scan. Further cooling/heating cycles show a similar behaviour.

In the initial heating from 300 to 400 K, compound **2** shows a classical semiconducting behaviour above *ca*. 360 K with an activation energy of *ca*. 2.0 eV (Figure S15b). After heating at 400 K the sample shows a quasi-metallic behaviour in the temperature range 400-225 K. Below the minimum in the resistivity plot at *ca*. 225 K the sample shows a smooth increase of ρ with decreasing the temperature that does not obey the Arrhenius law: $\sigma = \sigma_0 \exp(-E_a/kT)$, but rather a variable range hopping model for 1D systems in the temperature region *ca*. 225-20 K: $\sigma = \sigma_0 \exp[-(T_0/T)^{\alpha}]$ with $\sigma_0 = 0.032(2)$ S cm^{-1}, $T_0 = 2187(72)$ K and $\alpha = 0.51(1)$, a value very close to the expected one for a 1D system ($\alpha = 1/2$) (Solid line in Figure S15c).

This unusual huge increase of three orders of magnitude of the conductivity (from *ca*. 3×10^{-7} to *ca*. 3×10^{-4} S cm^{-1}) observed in compound **2** at 400 K indicates that this compound suffers a fast transformation to a much more conductive phase upon heating. Furthermore, after heating at 400 K the sample shows a quasi-metallic behaviour in the range 400-225 K and an activated conductivity with a 1D variable range hoping mechanism. This behaviour is very similar to the one observed in the closely related compounds $[CuI(L)]_n$ with L = EtIN and MeIN.[6] As in these two examples, the huge increase in the conductivity observed at high temperatures may be attributed to a partial reduction of the Cu(I) centres to Cu(0) followed by an oxidation of the carboxylato groups to CO and CO_2. The reduction of Cu(I) to Cu(0) is expected to drastically increase the conductivity of the crystal, as observed in **2** and in compounds $[CuI(L)]_n$ with L = EtIN and MeIN.

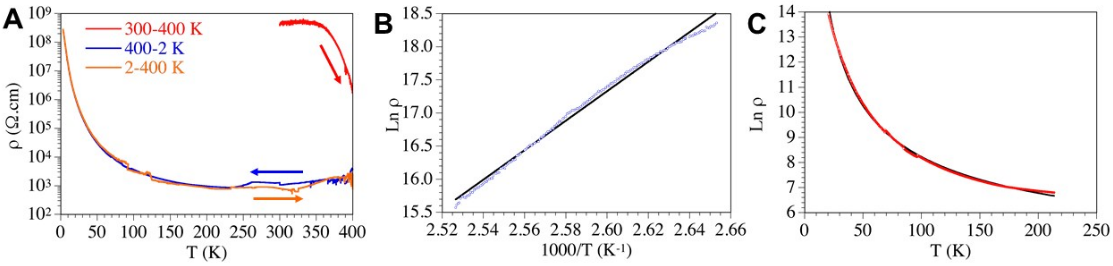

Figure S15. (a) Thermal variation of the electrical resistivity for compound **2**. (b) Arrhenius plot of compound **2** in the initial heating scan from 380 to 400 K. (c) Thermal variation of the electrical conductivity of compound **2** in the cooling scan after the initial heating at 400 K. Solid black line is the fit to the variable range hoping model.

The difference in conductivity values obtained at 25 °C for both compounds can be explained by observing the Cu-Cu distances of their structures at the same temperature. In case of compound $[Cu(MeIN)I]_n$ (**1m)**, the average Cu-Cu bond distance is 2.787Å whereas, in compound $[Cu(NH_2\text{-}MeIN)I]_n$ (**2m)**, which has a conductivity value of 5 orders of magnitude lower, the average Cu-Cu bond distance is longer (3.098 Å) which would explain this worse conductivity.

S6. Computational Methods

S6.1 Computed Density of Electronic States

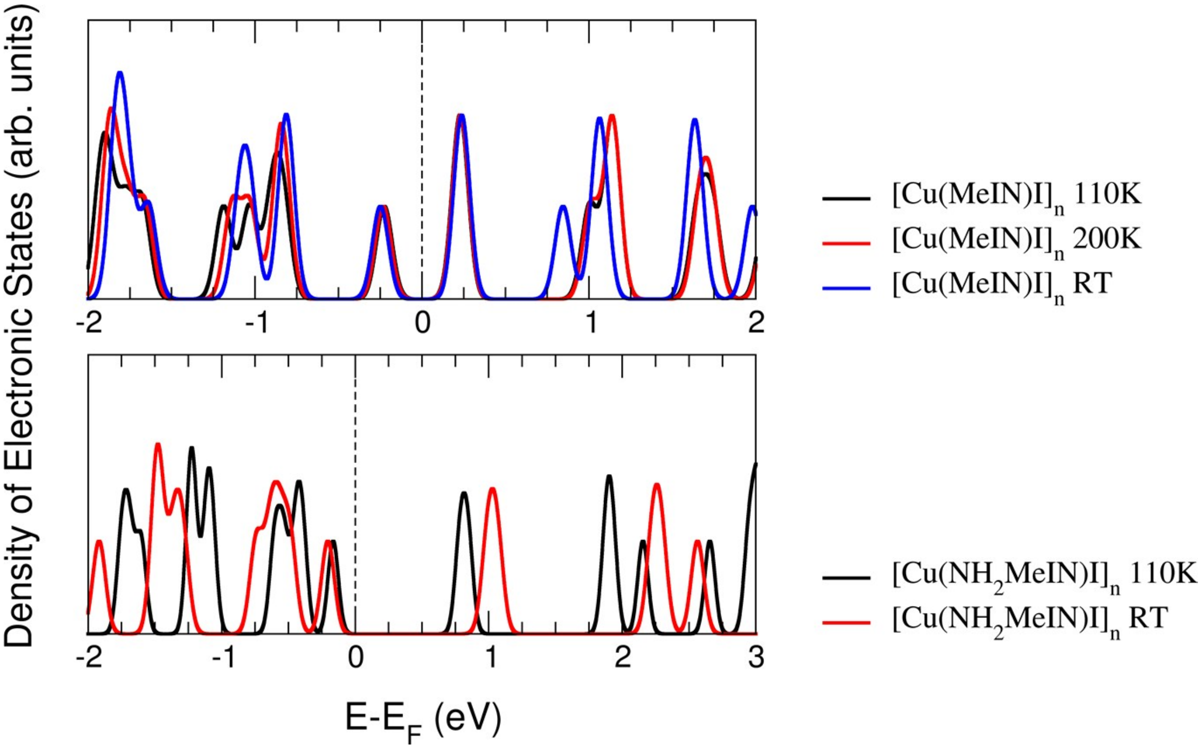

Figure S16. Computed density of electronic states (in arb. units) for the [Cu(MeIN)I]$_n$ (top panel) and [Cu(NH$_2$MeIN)I]$_n$ (bottom panel) compounds as a function of the energy referred to the Fermi level (in eV), for different temperatures (T=110, 200 and 296 K for [Cu(MeIN)I]$_n$ and T=110 and 296 K for [Cu(NH$_2$MeIN)I]$_n$. Different structures obtained by X-ray diffraction resolved at the given temperatures.

As observed in top panel of Figure S16, for [Cu(MeIN)I]$_n$ theory predicts a canonical narrow-gap semiconducting character for the three different structures at the different temperatures. For this polymer, neither an n-type nor p-type character can be categorically assigned since the Fermi level is located at the mid-gap. On the other hand, the global DOS profile morphology for all the three cases remains with no significant variations, excepting slightly for energies out from the gap region, which evinces that the structural changes induced by the increasing temperature do not substantially affect the electronic structure. In particular, the VB and CB remain practically unaltered and, thus, the electronic band-gap as well, with a value of 0.47 eV. Nevertheless, a more pronounced effect induced by the temperature is observed in the DOS profiles for [Cu(NH$_2$MeIN)I]$_n$ (bottom panel of Figure S16). In this case, not only do evident shifts between electronic states appear for the two temperatures, but also does a visible reduction of the band-gap from 1.25 eV at RT down to 0.92 eV at T=110 K. This observation will be directly related with the thermochromic effect observed for this compound, not observed for the previous [Cu(MeIN)I]$_n$ case.

S7. Composites Thin Films Preparation and Characterization

Preparation of films by slow evaporation: The hybrid materials films were obtained after evaporation of excess solvent of the previously prepared solutions of **2n** and PVDF at 25ºC heating at 75ºC for 1 hour.

Preparation of thin films by Dip-coating: The hybrid materials thin films were obtained after submerging a doped SiO_2 substrate in the previously prepared solutions of **2n** and PVDF, with a descending speed of 10 mm/min for 2 minutes, keeping the surface in the solutions for 2 minutes, and ascending at 10 mm/min for 2 more minutes.

Preparation of thin films by Spin-coating: The hybrid materials thin films were obtained by depositing a 15 µL drop of the previously prepared solutions of **2n** and PVDF on a doped SiO_2 substrate and rotating it on a Dremmel spin-coater at 1020 rpm for 30 seconds.

IR, PXRD and TGA data confirmed the presence of **2n** in the films (Figures S17-S20).

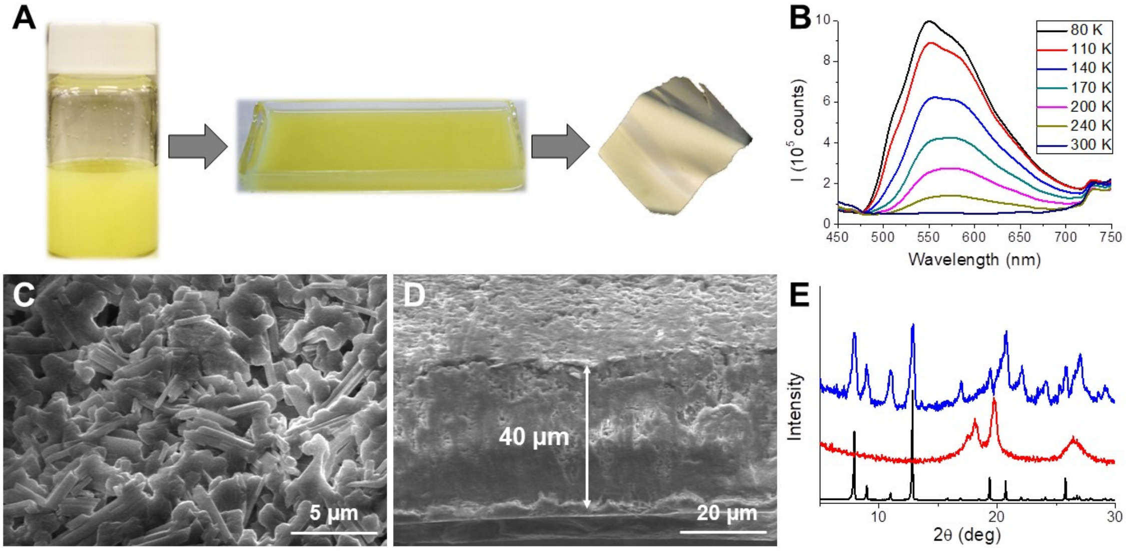

Figure S17. (a) Scheme of the slow-evaporation synthesis (DMF suspension) of the **2@PVDF** hybrid materials. (b) Luminescence spectra of the **2@PVDF** film, with 30% wt of **2**, at several temperatures (λ_{exc} = 375 nm). (c, d) SEM images of the **2**@PVDF film, with 30 % wt of **2**. (e) PXRD diffractograms of **2** (black), PVDF (red) and the **2**@PVDF film, with 30 % wt of **2** (blue).

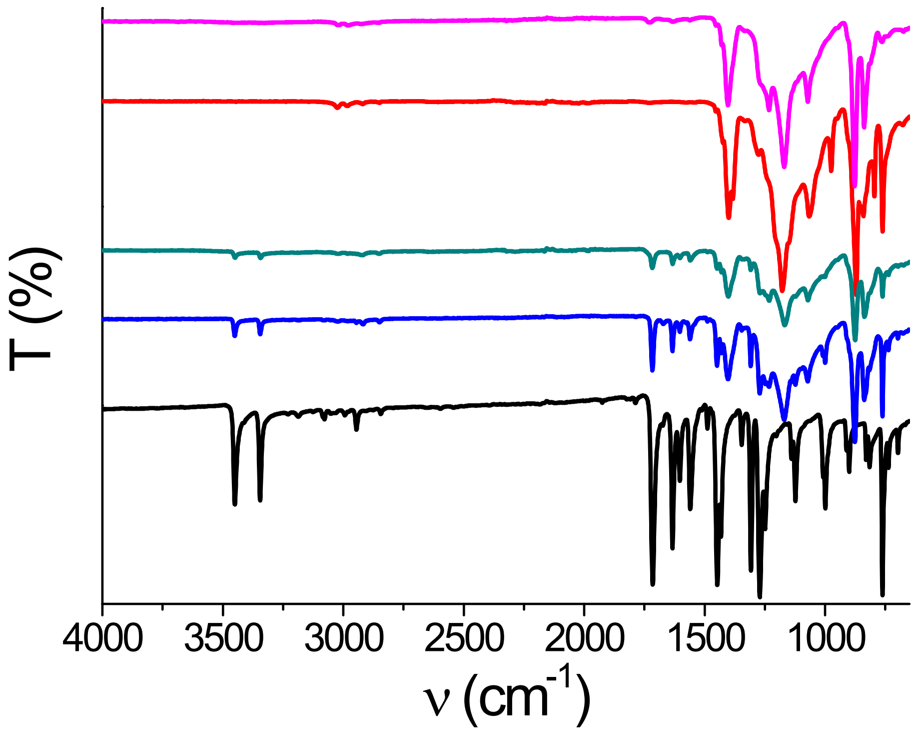

Figure S18. IR spectra of pristine **2** (black), **2@PVDF** films with 30% (blue), 15% (green) and 4% wt of **2** (pink), and of pristine PVDF (red).

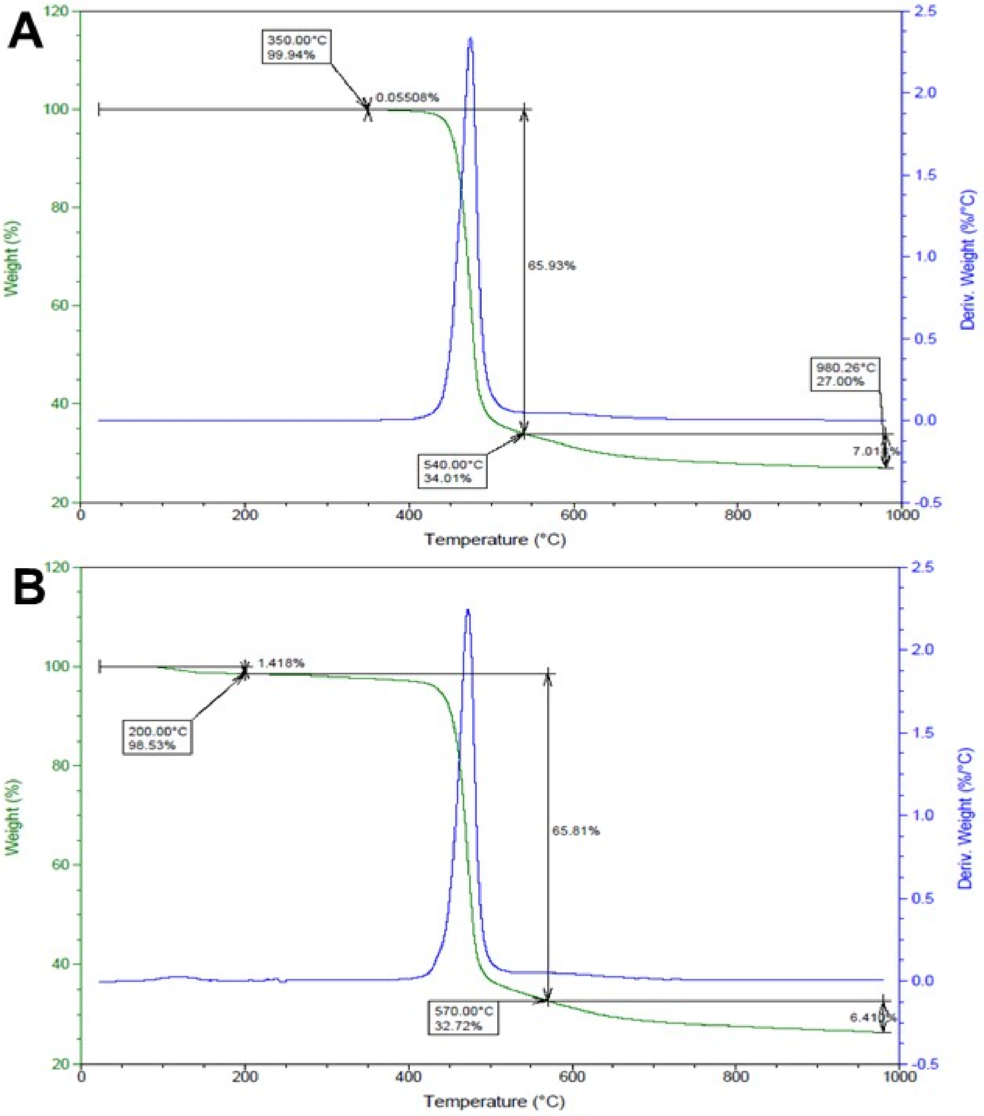

Figure S19. Thermogravimetric analysis of PVDF (a) and **2@PVDF** film with 4% wt of **2** (b), under nitrogen gas with flow rate 90 mL/min and heating rate 10 ºC/min. PVDF fully decomposes between 400 and 600 ºC; therefore, about 70% of the carbon remains as a residue (100% would suppose 37.5% of the total mass of PVDF). **2@PVDF** films show the decomposition patterns of both **2** (Figure S11) and PVDF.

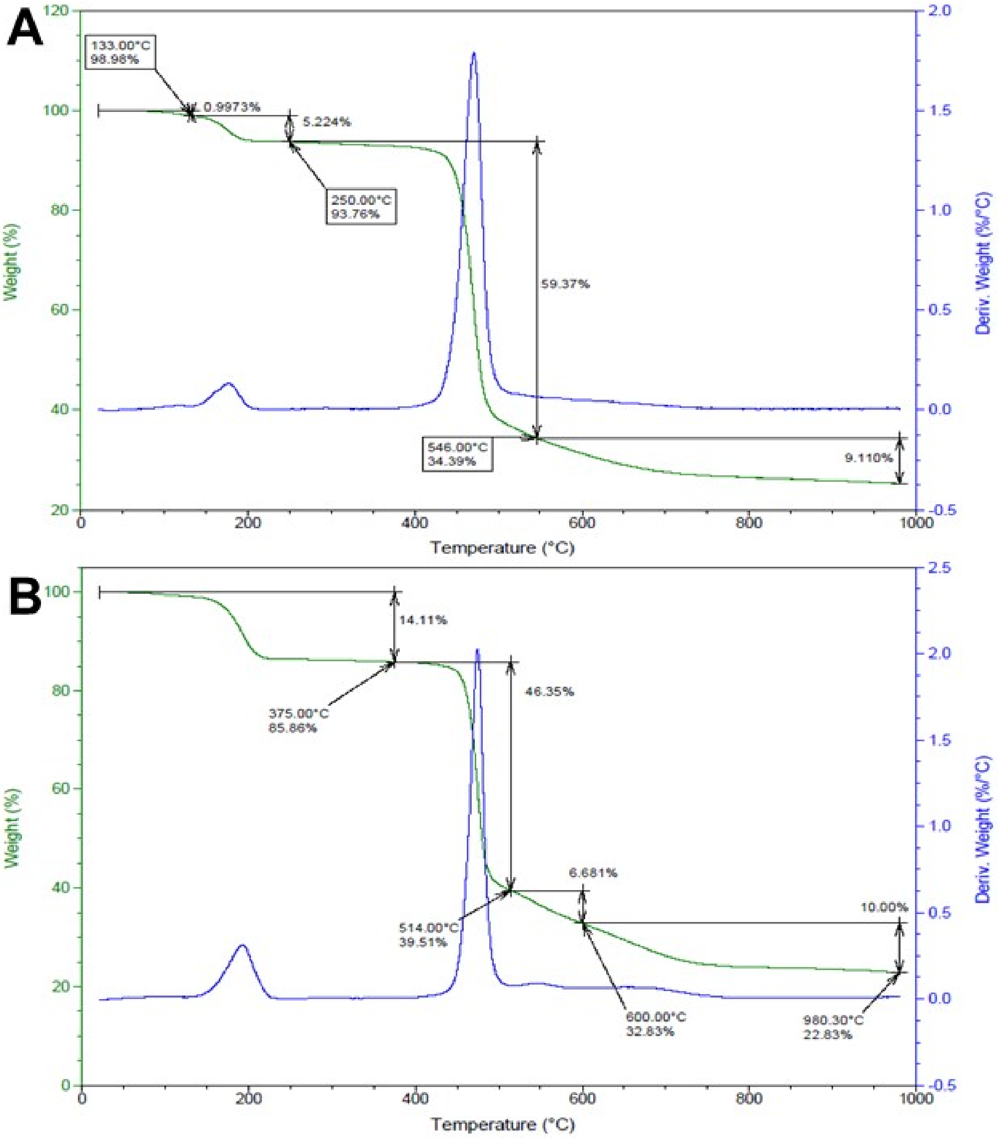

Figure S20. Thermogravimetric analysis of **2@PVDF** films with 15% (a) and 30% wt of **2** (b), under nitrogen gas with flow rate 90 mL/min and heating rate 10 ºC/min. PVDF fully decomposes between 400 and 600 ºC; therefore, about 70% of the carbon remains as a residue (100% would suppose 37.5% of the total mass of PVDF). **2@PVDF** films show the decomposition patterns of both **2** (Figure S11) and PVDF.

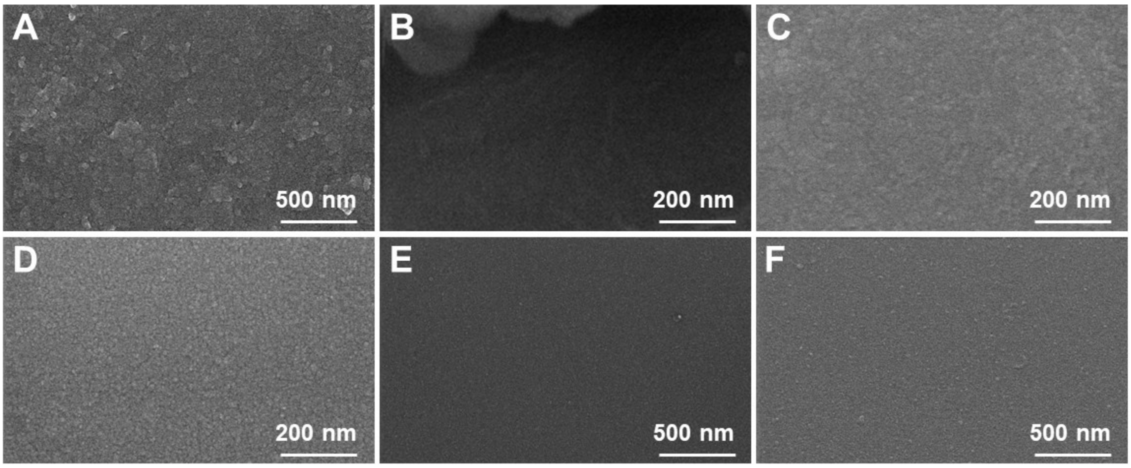

Figure S21. (a-c) SEM images of the dip-coating prepared **2n@PVDF** films with 4% (a), 15% (b) and 30% wt (c) of **2n**. (d-f) SEM images of the spin-coating prepared **2n@PVDF** films with 4% (d), 15% (e) and 30% wt (f) of **2n**.

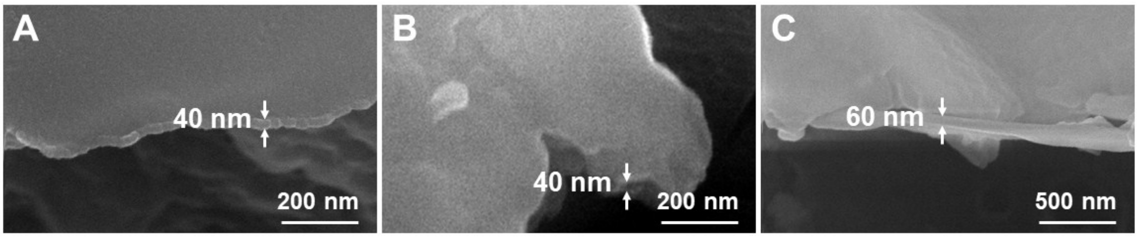

Figure S22. (a-c) SEM images of the edges of the dip-coating prepared **2n@PVDF** films with 4% (a) and 15% wt (b) of **2n**, and of the spin-coating prepared film with 30% wt of **2n** (c).

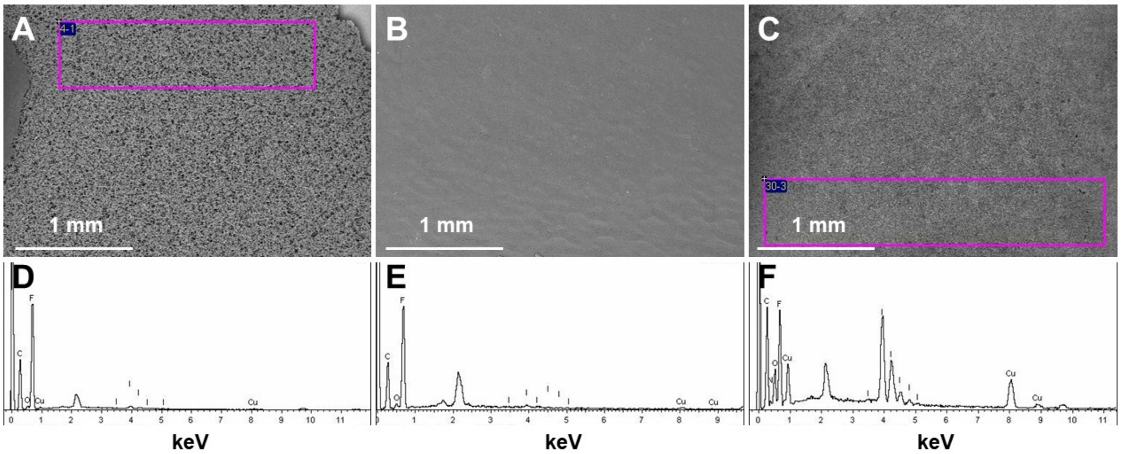

Figure S23. (a-c) Retrodispersed SEM images of the slow-evaporation synthesized **2@PVDF** films with 4% (a), 15% (b) and 30% wt (c) of **2n**. (d-f) EDX analyses of **2n@PVDF** films with 4% (d), 15% (e) and 30% wt (f) of **2n**. The analyses show that Cu and I are always in 1:1 proportions.

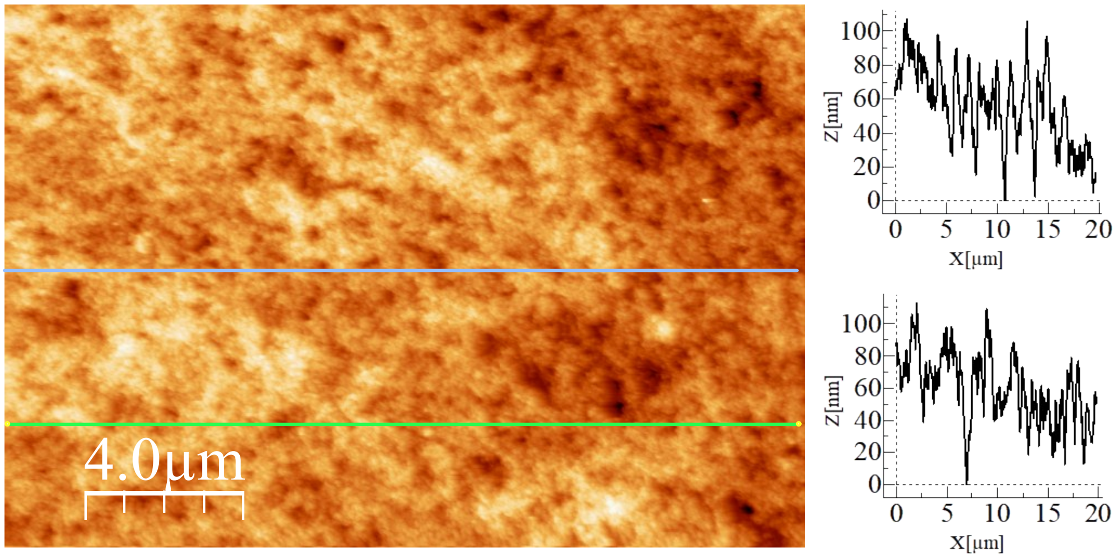

Figure S24. AFM images of an inner region of the **2@PVDF** film with 4 %wt of **2**, with their height profiles across the lines.

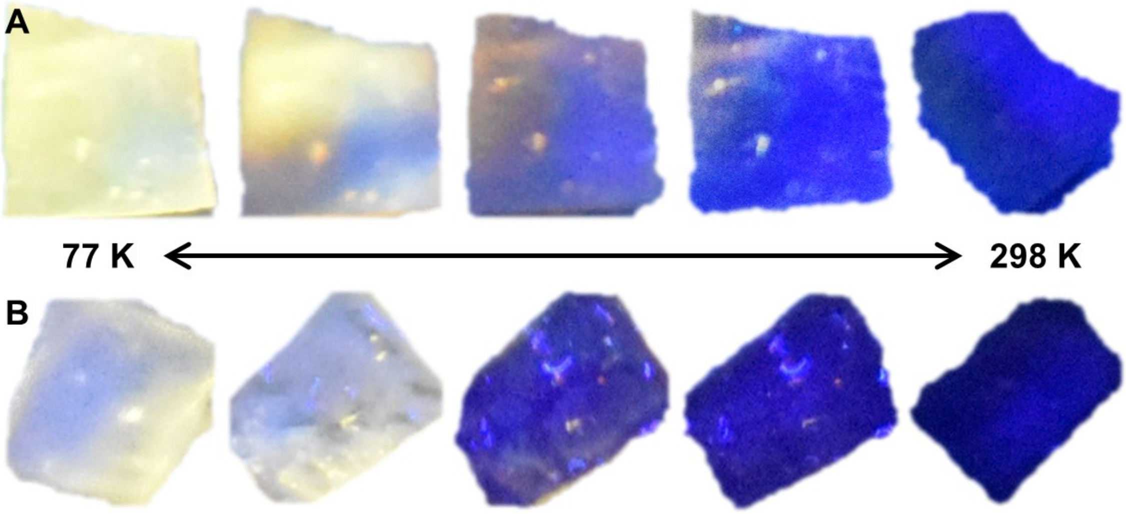

Figure S25. Thermoluminescent behavior of **2n@PVDF** thin film with 30 % wt of **2n** before (a) and after applying a 5 GPa pressure (b). λ_{exc} = 312 nm.

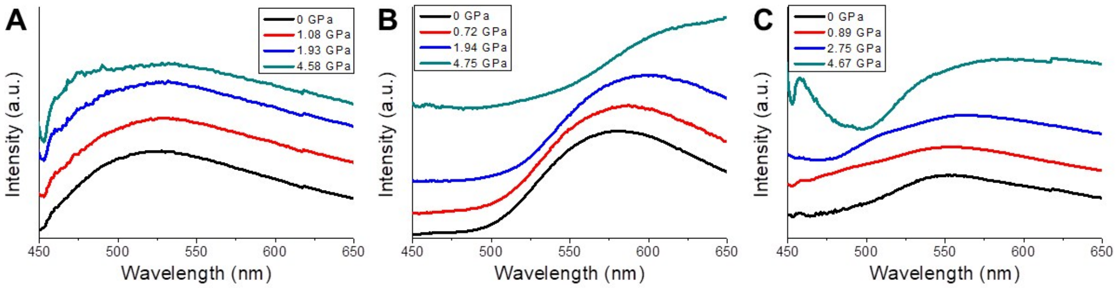

Figure S26. Luminescence spectra of the **2n@PVDF** thin films with 4 % (a), 15 % (b) and 30 % wt (c) of **2n** at different pressures (λ_{exc} = 375 nm).

S8. Experimental Methods

S8.1. Materials and Methods.

All reagents and solvents purchased were used without further purification. $[Cu(MeIN)I]_n$ (MeIN= methyl isonicotinate) (1) was prepared following the procedures already reported.[6] IR spectra were recorded with a PerkinElmer 100 spectrophotometer using a universal ATR sampling accessory from 4000–650 cm^{-1}. Elemental analyses were performed with a LECO CHNS-932 Elemental Analyser. Powder X-ray diffraction data was collected using a Diffractometer PANalyticalX'Pert PRO θ/2θ primary monochromator and detector with fast X'Celerator. The samples have been analysed with scanning θ/2θ.

Preliminary direct current (DC) electrical conductivity measurements were carried out on different single crystals of compound $[Cu(NH_2\text{-}MeIN)I]_n$ (2) with graphite paste at 300 K and two contacts. The contacts were made from tungsten wires (25 μm diameter). The samples were measured at 300 K by applying an electrical current with voltages from +10 to -10 V. The measurements were performed in the compounds along the crystallographic *a* axis. The thermal dependence of the dc electrical conductivity was measured with the four (or two, depending on the size of the crystal) contacts method on up to four single crystals of the compound[43] in the temperature range 2–400 K. The contacts were made with Pt wires (25 μm diameter) using graphite paste. The samples were measured in a Quantum Design PPMS-9 equipment connected to an external voltage source (Keithley model 2450 source-meter) and amperometer (Keithley model 6514 electrometer). All the quoted conductivity values were measured in the voltage range where the crystals are Ohmic conductors. The cooling and warming rates were 1 and 2 $Kmin^{-1}$.

Luminescence excitation and emission spectra of the solid methyl 2-aminoisonicotinate were performed at 298 ºC on a 48000s (T-Optics) spectrofluorometer from SLM-Aminco. A front-face sample holder was used for data collection and oriented at 608 to minimize light scattering from the excitation beam on the cooled R-928 photomultiplier tube. Appropriate filters were used to eliminate Rayleigh and Raman scatters from the emission. Excitation and emission spectra were corrected for the wavelength dependence of the 450 W xenon arc excitation but not for the wavelength dependence of the detection system. Spectroscopic properties were measured by reflection (front-face mode) on finely ground samples placed in quartz cells of 1 mm path length. No attempt was made to remove adsorbed or dissolved molecular oxygen from the materials. Reference samples that do not contain any fluorescent dopant were used to check the background and optical properties of the samples.

The thermal dependence of the luminescence emission spectra of compounds 1 and 2 and their emission lifetime were performed with a Jobin-Yvon Horiba Fluorolog FL-3-11 spectrometer using band pathways of 3 nm for both excitation and emission. Phosphorescence lifetimes were recorded with an IBH 5000F coaxial nanosecond flash lamp. Fluorescent lifetimes with a Data station HUB-B with a nanoLED controller and DAS6 software. The lifetime data were fitted with the Jobin-Yvon software package. Measurements at variable temperature were done with an Oxford Cryostat Optistat DN. The lifetime data were fitted using the Jobin-Yvon IBH software DAS6 v6.1.

The mechanical dependences of the luminescence emission spectra of compounds 1 and 2 were recorded exciting either with 375 nm or 457 nm diode lasers, respectively, using a 0.75 m single grating monochromator (Spex 750M) equipped with a cooled photomultiplier tube (Hamamatsu 928b). All spectra have been corrected for the instrument response. High pressure was generated with a miniature diamond anvil cell (mini-DAC), designed at The University of Paderborn (Germany), with low luminescent II-a type diamonds for optical, infrared and diffraction measurements. A stainless-steel gasket was pre-indented to 80 μm and a centred hole of typical diameter of 150 μm constitutes the sample chamber. Ruby chips were used as pressure calibrant using the ruby R_1line fluorescence and 16:3:1 methanol-ethanol-water mixture as pressure medium that provided hydrostatic pressures up to 14 GPa.[5]

Scanning Electron Microscopy (SEM) images were taken in a Philips XL 30 S-FEG electron microscope, applying an electron beam of 300 μA intensity and 10.0 kV potential, at a pressure of 10^{-7} Pa. To obtain reproducible results, very flat substrates were used with precisely controlled chemical functionalities, freshly prepared just before the chemical deposition of the samples. Doped SiO_2 surfaces were sonicated in ultrasound bath (Elma, 37 kHz, 380 W), for 15 min in acetone and 15 min in 2-propanol, and then dried under an Argon flow. After sample preparation, the surfaces were metallized with a 10 nm thick Cr layer, at a pressure of 10^{-3} Pa. SEM-EDX images and EDX spectra were taken in a Hitachi S-3000N microscope with an ESED detector coupled to an INCAx-sight EDX analyser. For this technique, samples were metallized with a 15 nm thick Au layer, at a pressure of 10^{-3} Pa. Atomic Force Microscopy (AFM) images were registered in a Nanotec Electronica microscope, at room temperature and in an open atmosphere, using Olympus cantilevers with a constant nominal force of 0.75 N/m. Images were processed by the use of the WSxM program.[43,S5]

S8.2. X-Ray Data Collection and Crystal Structure Determination.

The X-ray diffraction measurements were done using an Rigaku SuperNOVA diffractometer equipped with an EOS detector (CCD) and Mo radiation micro-source (λ= 0.71073Å). All measurements were processed with the CrysAlisPro software.[S6] The structure of the compound at RT was determined by a dual-space algorithm using the SHELXT program[S7] and refinement was performed using SHELXL program[S8] against F^2 by full-matrix least-squares refinement. All non-hydrogen atoms were refined anisotropically and hydrogen atoms were included in the model at calculated positions and refined with a rigid model with their U_{iso} value to $1.2U_{eq}$ of their parent atoms. The PLATON program[S9] has been used for geometric calculations. For high-pressure measurements, we have used a Diacell Bragg-S diamond anvil cell (DAC) from Almax-EasyLab, with an opening angle of 90° and anvil culets of 600 μm diameter, fitted with a stainless gasket containing a hole of 220 μm diameter and 50 μm depth. A methanol-ethanol-water mixture (16:3:1) was used as pressure-transmitting medium, which remains hydrostatic in the range of pressure used in our experiments.[48,S10] In order to minimize deviatory stresses which can cause incorrect values for bulk modulus.[S11] The sample was placed on one of the diamond anvils (diffraction side) together with a small ruby sphere as pressure sensor. The structure was refined, for each pressure, using previous results as starting point, on F^2 by full-matrix least-squares refinement using the SHELXL program. Due to limitations of the opening angle of our DAC it is only possible to collect about 35% of the total reflections present in a full dataset at ambient conditions. In this situation, structure refinements were performed with isotropic displacement parameters for all atoms except for the heavy atoms (Cu and I) that were refined with anisotropic displacement parameters whenever they did not become non-positive definite. Hydrogen atoms were included in the final procedure in the same way as for ambient conditions. No restraints were used during this process. Crystallographic data for the structures reported in this contribution have been deposited with the Cambridge Crystallographic Data Centre as supplementary publication 1826856-1826858.

S8.3. Theoretical Methodology.

These calculations have been used to compute mechanical and electronic properties, total energies, density of electronic states profiles and excitation spectra in the visible region. An efficient TDDFT formalism has been used to calculate the excitation spectra[S12-S17] as implemented within the plane wave (PW) basis set within the QUANTUM ESPRESSO distribution (http://www.quantum-espresso.org). In the calculations we have used the simulation cells and structures as obtained by X-ray diffraction experiments (for different T and P conditions), yielding residual forces acting on each atom below 0.1 eVÅ^{-1}, sufficient to guarantee fully converged results. Spin-polarized calculations did not show any significant variation with respect to the spin-unpolarised tests. In all the calculations the Brillouin zones (BZs) were sampled by means of optimal Monkhorst–Pack grids.[S18] We used the Perdew–

Burke–Ernzerhof (PBE) XC-GGA functional, ultra-soft pseudopotentials[S19] and a PW's basis set up to a kinetic energy cut-off of 40 Ry, as well as 300 Ry for the charge density. The excitation spectra are calculated as: $I(\omega) \propto \omega \mathrm{Im}[\alpha(\omega)]$, where α is the spherical average (average of the diagonal elements) of the dipole polarizability; an imaginary part of 0.002 Ry has been added to the frequency in order to smooth the emerging divergences of the polarizability. Additionally, once the different TDDFT spectra were obtained as aforementioned, we have carried out a battery of calculations with the GAUSSIAN09 package[S20] to obtain oscillator strengths, and elucidate transitions and electronic states involved in the most intense excitations by using the same GGA-PBE functional and the rather large 6-311G$*$ basis set. To compute the individual transitions we have made use of the configuration interaction singles (CIS) method,[S21] which requests a calculation on excited states using single-excitation CI (CI-Singles). This implementation provides excellent results in both closed-shell and open-shell systems.

S8.4. Synthesis of $[Cu(MeIN)I]_n$ (1).

Copper(I) iodide (201 mg, 1.05 mmol) was dissolved in 15 mL of acetonitrile. Methyl isonicotinate (126 µL, 1.07 mmol) was added to the mixture; instantly, the solution turned orange, and an orange solid precipitate. The solid was immediately filtered, washed with methanol (2 x 3 mL) and dried in vacuum (Yield: 170 mg; 49 % based on Cu). 1m: Single-crystals were formed upon standing the mother orange solution (obtained after filtration of 1n) at 25 ºC for 72 h. The orange crystals obtained were filtered off, washed with methanol (2 x 3 mL) and dried in vacuum (Yield: 59 mg; 17 % based on Cu).

Elemental analysis calcd (%) for $C_7H_7CuINO_2$: C 25.66, H 2.15, N 4.28; found: C 25.72, H 2.15, N 4.28; IR selected data (ATR): n (cm^{-1}) = 3039 (vw), 2950 (w), 1728 (vs), 1560 (w), 1433 (m), 1414 (m), 1321 (m), 1288 (s), 1184 (w), 1119 (m), 1061 (w), 955 (w), 854 (w), 758 (m), 700 (m), 690 (m). DRX powder diffraction data of 1n and 1m confirm their purity (Figure S7).

S8.5. Synthesis of $[Cu(NH_2\text{-}MeIN)I]_n$ (2).

Copper(I) iodide (100 mg, 0.53 mmol) was dissolved in 8 mL of acetonitrile at 20 ºC, and methyl 2-aminoisonicotinate (NH_2-MeIN) (81 mg, 0.53 mmol) was dissolved in 8 mL of ethanol at 50 ºC. Then, both solutions were mixed at 25 ºC under magnetic stirring (500 rpm). A pale-yellow solid is immediately formed, filtered off, washed with acetonitrile (2 x 5 mL), ethanol (2 x 5 mL) and diethyl ether (2 x 3 mL), and dried in vacuum (Yield: 85 mg; 50 % based on Cu). 2m: Single-crystals were formed upon standing the mother yellow solution (obtained after filtration of 2n) at 25 ºC for 48 h (Yield: 43 mg; 25 % based on Cu).

Elemental analysis calcd (%) for $C_7H_8CuIO_2N_2$: C 24.52, H 2.34, N 8.17; found: C 24.96, H 2.34, N 8.07; IR selected data (ATR): n (cm^{-1}) = 3450 (s), 3345 (s), 3186 (w), 3078 (w), 2992 (w), 2945 (w), 2845 (w), 1788 (w), 1716 (vs), 1634 (vs), 1603 (m), 1560 (vs), 1489 (w), 1448 (vs), 1432 (s), 1346 (m), 1308 (vs), 1270 (vs), 1249 (s), 1123 (s), 999 (s), 900 (m), 830 (w), 816 (m), 762 (vs), 737 (m), 697 (w). DRX powder diffraction data of 2n and 2m confirm their purity (Figure S8).

S8.6. SEM samples preparation.

30 mg of polycrystalline 1n or 2n were redispersed in 5 mL of water, and 20 µL of the suspension were deposited on a doped SiO_2 surface; the drop was left to adsorb for 3 min. and dried with an Argon flow.

S8.7. AFM samples preparation.

1n: Copper (I) iodide (200 mg, 1.05 mmol) was dissolved in 15 mL of acetonitrile. Under magnetic stirring (500 rpm), methyl isonicotinate (124 µL, 1.05 mmol) was added, immediately an orange solution was formed and, after 1 min., a dense orange suspension. 1 mL portion of this suspension was centrifuged (5 min., 10000 rpm) and washed with methanol (2 x 1 mL). The solid was redispersed in 1 mL of methanol, and 40 µL of this suspension was mixed with 3960 µL milli-Q-water water (dilution: 10^{-2}; final concentration: $7 \cdot 10^{-4}$ M). A drop (15 µL) of the new suspension was deposited onto doped SiO_2, allowing adsorption for 1 min. After this, the surface was dried with an argon flow.

2n: Copper(I) iodide (100 mg, 0.53 mmol) was dissolved in 8 mL of acetonitrile; on the other hand, methyl 2-aminoisonicotinate (NH_2-MeIN) (81 mg, 0.53 mmol) was dissolved in 8 mL of ethanol, at 50 ºC. Both solutions were mixed at 25 ºC and magnetically stirred (500 rpm), observing the immediate formation of a yellowish solution and a pale yellow solid consisting of $[Cu(NH_2\text{-MeIN})I]_n$ nanofibers. 1 mL of this suspension was centrifuged (5 min., 10000 rpm) and washed with ethanol (2 x 1 mL). The solid was redispersed in 1 mL of ethanol. *Dip-Coating deposition*: 50 µL of the ethanol suspension were dispersed in 4.950 mL of milli-Q water (dilution: 10^{-2}; final concentration: $7 \cdot 10^{-4}$ M). This diluted suspension was deposited on a doped SiO_2 surface by dip-coating, with a descending speed of 10 mm/min. for 2 min., keeping the surface in the suspension for 2 min., and ascending at 10 mm/min. Then the surface was dried under an argon flow. *Drop-Casting deposition*: 10 µL of the ethanol suspension were dispersed in 9.990 mL of milli-Q water (dilution: 10^{-3}; final concentration: $7 \cdot 10^{-5}$ M). 20 µL of the diluted suspension were deposited on a doped SiO_2 surface and left to adsorb for 1 min.; after that, the surface was dried under an argon flow.

S8.8. Preparation of 2@PVDF Thin Films.

Polyvinylidene difluoride (PVDF) polymer was doped with compound $[Cu(NH_2\text{-MeIN})I]_n$ (2n) in 4, 15 and 30% (wt). Compound 2n was dispersed in acetone, and PVDF was dissolved in DMF. Both components were mixed in different proportions and dispersed with sonication for 30 min., allowing an almost total solution of 2n. The resulting homogeneous suspension was used to prepare different-sized 2n@PVDF films: thicker ones were prepared by casting the suspension on microscope slides and drying at 75 ºC for 1 h to remove DMF; the films were delaminated via immersion in water and dried in air. Thin films were prepared by depositing the suspension on SiO_2 surfaces by dip-coating for 2 min. or spin-coating for 30 sec. at 1020 rpm and dried with an Argon flow. IR, PXRD and TGA data showed the presence of 2n in the films (Section S7, Figures S17-S20).

Supplementary References

S1. M. Knorr, F. Guyon, A. Khatyr, C. Daschlein, C. Strohmann, S. M. Aly, A. S. Abd-El-Aziz, D. Fortin and P. D. Harvey, *Dalton Trans.*, 2009, 948.

S2. F. Allen, *Acta Cryst. Sect. B*, 2002, **58**, 380.

S3. J. Gonzalez-Platas, M. Alvaro, F. Nestola and R. Angel, *J. Appl. Cryst.*, 2016, **49**, 1377.

S4. R. J. Angel, Win_Strain program for Strain calculations *(http://www.rossangel.net)*, 2015.

S5. M. Usman, S. Mendiratta and K. L. Lu, *Adv. Mater.*, 2017, **29**, DOI 10.1002/adma.201605071.

S6. Rigaku Oxford Diffraction, CrysAlisPro Software system, version 1.171.38.41 (Rigaku Corporation), 2016.

S7. Y. H. Luo, H. W. Liu, F. Xi, L. Li, X. G. Jin, C. C. Han and C. M. Chan, *J. Am. Chem. Soc.*, 2003, **125**, 6447.

S8. J. M. González-Pérez, C. Alarcón-Payer, A. Castiñeiras, T. Pivetta, L. Lezama, D. Choquesillo-Lazarte, G. Crisponi and J. Niclós-Gutiérrez, *Inorg. Chem.*, 2006, **45**, 877.

S9. A. Spek, *Acta Cryst. Sect. D*, 2009, **65**, 148.

S10. R. J. Angel, M. Bujak, J. Zhao, G. D. Gatta and S. D. Jacobsen, *J. Appl. Cryst.*, 2007, **40**, 26.

S11. D. Errandonea, A. Muñoz and J. Gonzalez-Platas, *J. Appl. Phys.*, 2014, **115**, 216101.

S12. D. Rocca, R. Gebauer, Y. Saad and S. Baroni, *J. Chem. Phys.*, 2008, **128**, 154105.

S13. B. Walker and R. Gebauer, *J. Chem. Phys.*, 2007, **127**, 164106.

S14. B. Walker, A. M. Saitta, R. Gebauer and S. Baroni, *Phys. Rev. Lett.*, 2006, **96**, 113001.

S15. S. Baroni, S. De Gironcoli, A. Dal Corso and P. Giannozzi, *Rev. Mod. Phys.*, 2011, **73**, 515.

S16. X. Gonze, *Phys. Rev. A*, 1995, **52**, 1096.

S17. S. Baroni, P. Giannozzi and A. Testa, *Phys. Rev. Lett.*, 1987, **58**, 1861.

S18. H. J. Monkhorst and J. D. Pack, *Phys. Rev. B*, 1976, **13**, 5188.

S19. D. Vanderbilt, *Phys. Rev. B*, 1990, **41**, 7892.

S20. M. J. Frisch, Gaussian 09, Revision E.01 (Gaussian, Inc.), 2009.

S21. S. Sakai, *J. Phys. Chem.*, 1992, **96**, 131.